Experimental investigation of the aerodynamic drag of roof-mounted insulators for trains

Jonathan Tschepe[1] ⓘ, Jörg-Torsten Maaß[2],
Christian Navid Nayeri[1] and Christian Oliver Paschereit[3]

Abstract

This paper presents the results of experimental investigations on the aerodynamic drag of roof-mounted insulators for use on low- and high-speed trains. Wind tunnel investigations at different Reynolds numbers in the subcritical, critical, and supercritical flow regime were performed, in addition to investigations using wall-mounted cylinders. Furthermore, the impact of insulator sheds made of flexible material was analyzed. For a better understanding of the aerodynamic behavior of the insulators when mounted on trains, different boundary conditions representing realistic configurations as found on the roof of trains were simulated. From the measured drag, the energy demand to overcome the aerodynamic resistance of different types of insulators was calculated. Depending on the above mentioned boundary conditions, a noticeable contribution of the insulators to the entire train's aerodynamic drag could be observed. With flexible insulator sheds, a further increased air resistance was observed with the onset of fluttering. Similar to the cylinder, the aerodynamic behavior of the insulators depends on the respective Reynolds number.

Introduction

The aerodynamic drag of trains contributes to about 20–50% of its energy demand, depending on the train's shape and speed.[1–3] In case of uncovered roof equipment, the pantograph and associated elements, such as insulators and surge arresters, are responsible for about 8% of the aerodynamic drag, depending predominantly on the number of elements and their arrangement on the roof.[4–7]

To the knowledge of the authors, so far only the pantograph itself has been investigated in detail with regard to its drag characteristics, while the insulators are supposed to behave in the same way as wall-mounted cylinders. Detailed investigations of such cylinders under different inflow conditions were performed, for example by Rosemeier,[8] Farivar,[9] Sumner et al.,[10] and Wang et al.[11] A good overview of further work was collected by Pattenden et al.[12] As observed for cylinders of quasi-infinite length,[13,14] for finite wall-mounted cylinders, a critical Reynolds number $Re_{D,crit}$ ($\equiv u_\infty D/\nu$, with u_∞ being the free-stream velocity, D the diameter, and ν the fluid viscosity) can as well be found, dividing the flow into different regimes. With $Re_{D,crit} \sim 1-2 \times 10^5$ this critical Reynolds

number for finite cylinders is about the same as for infinite cylinders[11,15] and is very sensitive to free-stream turbulence and surface roughness.[14] Below this critical Reynolds number, a subcritical flow regime characterized by laminar boundary layer flow and periodic alternating vortex shedding is found.[13] The drag coefficient C_D ($\equiv F_D/p_{dyn}A$, with F_D being the drag force normalized by the dynamic pressure p_{dyn} and a reference area A) in this regime is nearly constant. In the critical regime, up to about $Re_D \sim 4 \times 10^5$, a rapid decrease of the drag coefficient can be observed, due to a transition of the boundary layer and turbulent reattachment.[14] Above $Re_D \sim 4 \times 10^5$, a supercritical regime exists, characterized by a fully turbulent boundary layer flow and less regular vortex shedding behavior. The drag coefficient

[1]Berliner Institut für Technologietransfer, Berlin, Germany
[2]Bombardier Transportation, Hennigsdorf, Germany
[3]Institut für Strömungsmechanik und Technische Akustik, Technische Universität Berlin, Germany

Corresponding author:
Jonathan Tschepe, Berliner Institut für Technologietransfer, Pascalstr. 10, 10587 Berlin, Germany.
Email: tschepe@bit-berlin.de

again is nearly constant but at a significantly lower level than in the subcritical regime.[15,16] The distinct Reynolds number impact on the drag coefficient found for the bare cylinder has not been investigated for insulators or finned cylinders so far. Therefore, this is one aim of the current study.

The application of fins on cylinders of quasi-infinite length (as shown for a finite cylinder in Figure 4) has been mainly studied to investigate the impact of the fins on the vortex shedding and a possible flow stabilization.[17–19] McClure et al.[20] intensively studied the effect of fins with different spacing on the flow around an infinite cylinder. They showed that the flow around the finned cylinder is similar to the one around a bare cylinder. When the spacing between the fins s is larger than $s/D_1 > 0.4$, the flow structures (vortex shedding frequency, wake width and length) are similar to the ones of a bare cylinder with inner diameter D_1 (cf. Figure 4). For smaller spacing, the flow structures approach the ones of a bare cylinder with outer/fin diameter D_2. As fins are added to the base cylinder, the mean drag coefficient initially increases approximately linearly with increasing fin density. At $s/D_1 \sim 0.1$, a maximum (with a drag increase of about 100%) is reached and for closer spacing the drag coefficient appears to decrease again.

For the evaluation of the aerodynamic characteristics of finned cylinders, a meaningful definition of reference quantities for the calculation of nondimensional flow parameters, as e.g. the Reynolds number, is required. Based on the evaluation of the Strouhal number similarity, Mair et al.[17] suggested the use of an effective diameter D_{eff}

$$D_{eff} = D_1 + \frac{t}{s}(D_2 - D_1) \tag{1}$$

with D_1 being the inner diameter, D_2 the outer/fin diameter (as shown in Figure 4), and t the thickness of the fins. McClure et al.[20] suggested the use of more complex definitions taking into account also the boundary layer evolving on the fins. So far, all studies using finned cylinders have been performed in the subcritical Reynolds number regime.

Since the insulators are located on the roof of the train, the surrounding flow depends on the speed of the train and the boundary layer developing along the train. In addition, upstream elements can have an influence on the flow. Because the driving speed can be very different in case of a commuter or high-speed train, or in case of scaled model investigations, the Reynolds number impact is of interest. The boundary layer development along a train's roof is very dependent on its geometry and a general statement on the expected boundary layer thickness and profile therefore is difficult. Investigations by Takaishi[21] showed that on a smooth train the boundary layer thickness δ_{99} on the first 1–2 cars can be expected to be in the range of $\delta_{99} \sim 0.2$–0.5 m, while on cars 7–8 $\delta_{99} \sim 1$–2 m. On less streamlined trains,

an increased boundary layer thickness can be expected.[22] In case of shielding, cavities, etc., the near-wall momentum flux is further reduced, decreasing the aerodynamic forces on the respective element.[23] This being said, a number of different boundary conditions need to be investigated to evaluate the respective aerodynamic drag of an insulator mounted on a train roof.

This paper presents the results of investigations using different wall-mounted insulators and cylinders at subcritical, critical, and supercritical Reynolds number regimes. Different upstream flow conditions, i.e. boundary layer profiles and thicknesses, were analyzed. Furthermore, the impact of flexible insulator fins (in the following called sheds) was investigated. Flexible materials, such as silicone, are becoming more and more of use on train insulators due to safety reasons, reduced soiling, and improved insulation properties. However, under the influence of the head wind, the flexible sheds are expected to flutter. In order to evaluate such effects, different insulators with flexible sheds have been investigated in the wind tunnel.

Experimental setup

The investigations were performed in the high-speed test section of the large wind tunnel of the *Hermann-Föttinger Institute* of the *Technical University of Berlin*. The test section has a cross-section area of $2\,m \times 1.4\,m$ (width × height) and a length of $5\,m$. The maximum flow velocity in the test section was about $70\,m/s$. In the empty test section, the turbulence level was below 1%. The object under investigation was mounted on a six-component balance (*ME K6D80*, $1\,kN$ range, accuracy 0.1%) placed underneath the wind tunnel (Figure 1). In order to easily exchange the investigation object, a connection plate on which the objects could be mounted was installed $1.5\,mm$ above the wind tunnel floor. The drag of the single plate has been measured for all configurations and was subtracted from the drag of the investigation objects. A boundary layer rake as shown in Figure 1 was utilized to analyze the boundary layer thickness at the measurement location. The pitot tubes of the rake were connected to $2\,kPa$ differential sensors (*SensorTechnics HDO series*, accuracy 0.2%). The static reference pressure was taken from a Prandtl tube, which has been installed $0.2\,m$ upstream the measurement position at $0.25\,m$ distance from the upper wall, thus being safely outside the wall boundary layer. The Prandlt tube was also used to detected the flow velocity. The dynamic pressure p_{dyn} of the Prandtl tube was measured by a Baratron of type *MKS 220CD-00100D2BS*, with a range of $\pm 10\,kPa$ and an accuracy of 0.15%. The flow velocity u was calculated from the dynamic pressure using

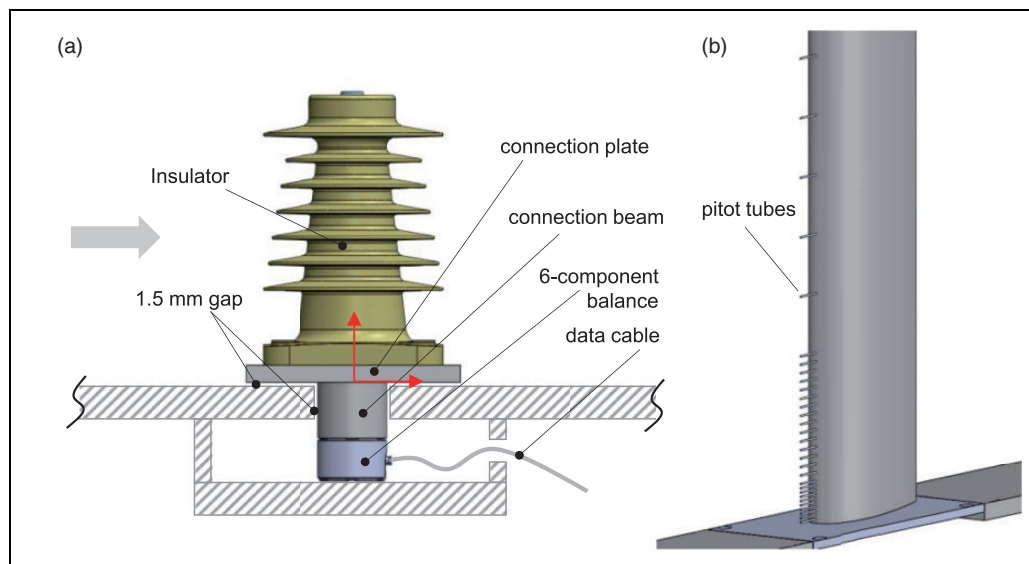$$u = \sqrt{\frac{2}{\rho} p_{dyn}} \tag{2}$$

Figure 1. Experimental setup for (a) force measurements and (b) boundary layer measurements.
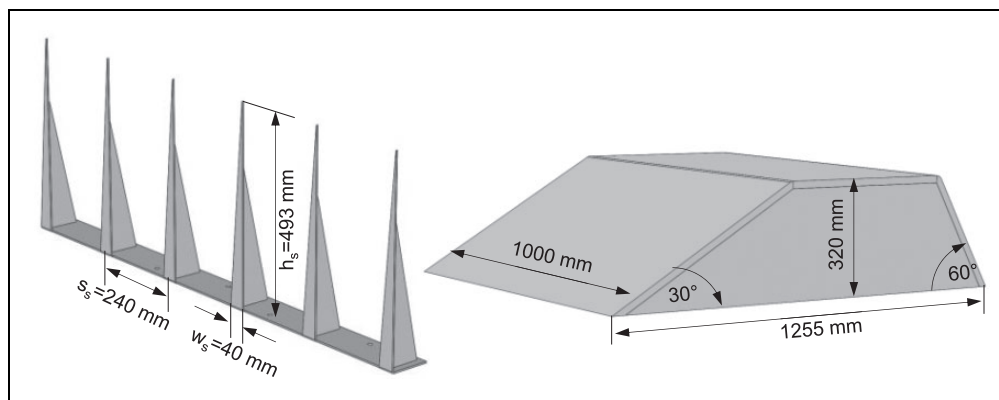

Figure 2. Dimensions of the spires (left) and the generic roofbox (right).

The air density ρ was determined from the humidity, temperature, and pressure measured inside the wind tunnel. All data were recorded using 16 Bit *9223 cDAQ* modules from *National Instruments* with a sampling frequency of 10 kHz over a time span of 25 s. For the subsequent analysis, all data were averaged. The uncertainty for C_D was calculated to be within $\pm 1\%$ for $Re > 4 \times 10^5$ and within $\pm 5\%$ for lower Reynolds numbers, due to the precision of the force sensor. The uncertainty for the Reynolds number is within $\pm 0.3\%$.

In order to simulate different flow situations as can be found on trains, spires to increase the boundary layer thickness and a generic roofbox, mounted at different locations upstream the investigation objects, were used (Figures 2 and 3). The spires were designed according to Irwin,[24] aiming at generating a (turbulent) boundary layer thickness of 0.5 m. The roofbox was designed based on typical dimensions as found for different types of trains.

Insulators of different shapes and materials, such as cycloaliphatic epoxy resin (CER) or different types of

silicone coating (high-temperature-vulcanizing [HTV], room-temperature-vulcanizing [RTV], liquid silicone rubber [LSR]), were investigated (Figures 4 and 5 and Table 1). In order to compare the insulator's drag coefficient to the drag coefficient of simple cylinders, comparative investigations using cylinders with the inner and outer diameters of one specific insulator were conducted (Figure 4). Table 1 gives the dimensions of the different objects. For the insulators, in case of conical shapes the average diameter is given. The effective diameter D_{eff} was calculated by dividing the projected frontal area A_{proj} by the object's height H (Table 1). With regard to the non-homogenous distribution of the sheds, this approach appeared to be more appropriate than using equation (1) to ensure good comparability of different geometries.

Results

Velocity profiles

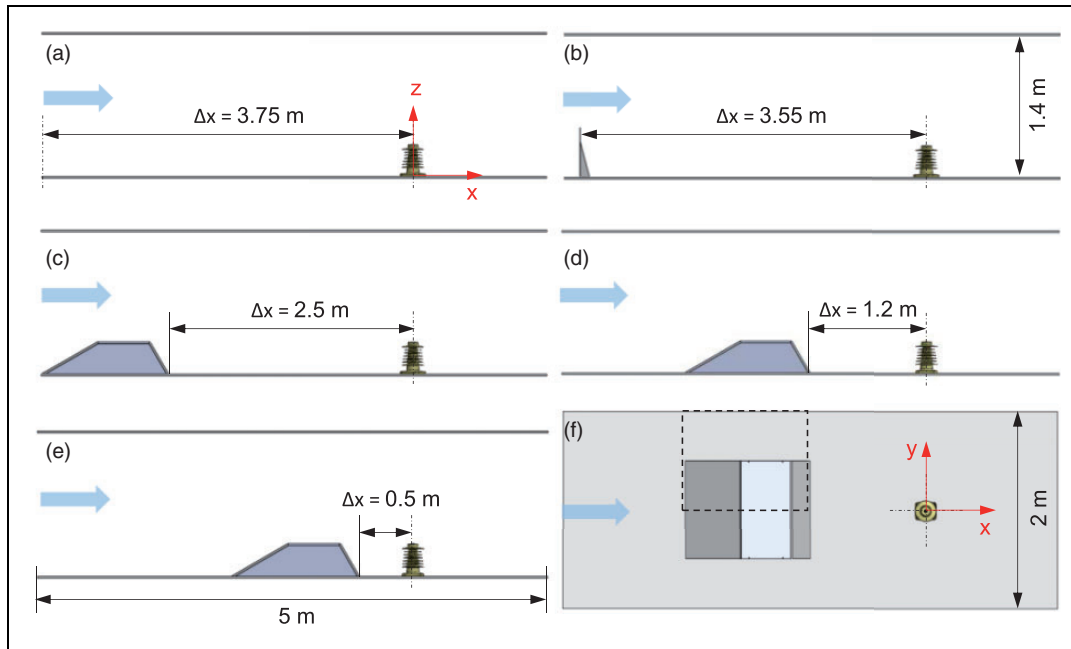Figure 6 shows the velocity profiles measured at $x = 0$ and $y = 0$ along the z-axis (cf. Figure 3).

Figure 3. Setup dimensions for different boundary conditions: (a) undisturbed flow; (b) with spires; (c) roofbox at x1; (d) roofbox at x2; (e) roofbox at x3; (f) top-view of roofbox at x2. Dashed lines indicate configuration of "roofbox x2 side".
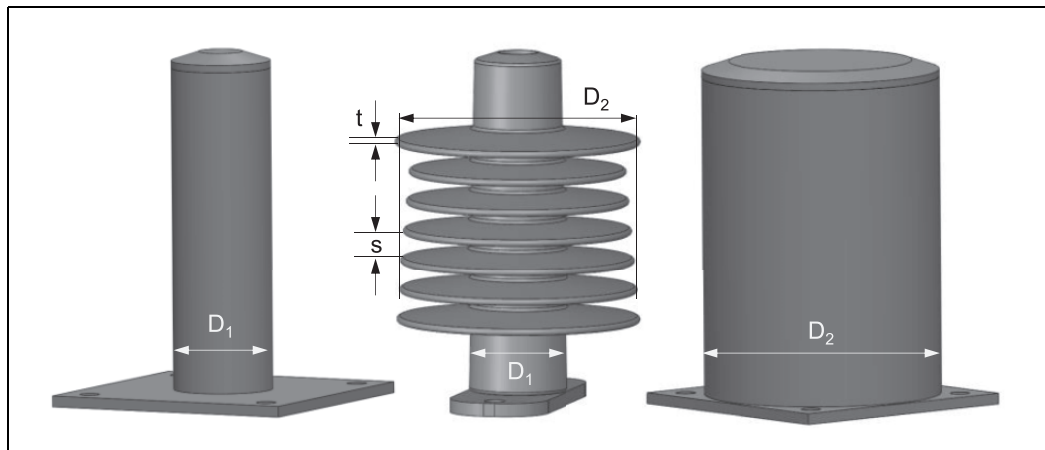

Figure 4. Insulator 1 with inner diameter D_1 and outer diameter D_2 and generic cylinders with respective diameters.

The boundary layer thickness δ_{99} is 0.12 m in the empty test section (undisturbed flow) and 0.48 m with the spires installed upstream. The latter approximately represents the roof boundary layer thickness found on the second or third car of a train,[21,22] depending very much on the train's shape. The boundary layer profile can be estimated using a theoretical power law formula[25]

$$\frac{u(z)}{u_\infty} = \left(\frac{z}{\delta_{99}}\right)^{\frac{1}{n}} \tag{3}$$

On the roof of trains, the velocity profiles correspond to the theoretical profiles when using $n = 7$ to $n = 11$.[22,26,27] Figure 6 shows that the velocity profile generated by the spires approximately agrees with the

theoretical profile for $n = 7$. The boundary layer profiles generated by the roofbox at x1 (2.5 m upstream the insulator) are similar to the profile generated by the spires, whereas the wake depression becomes more pronounced. At closer distance of the roofbox to the measurement location, the momentum in proximity of the wall is significantly reduced, and at x3 (0.5 m upstream the insulator) even backwash can be assumed. Since the pressure rake did not allow for the measurement of $u < 0$, the exact velocity profile for x3 in wall proximity could not be investigated. The velocity profile for the roof box at position x2 qualitatively agrees with the results presented by Carnevale[28] for a comparable situation. Therefore, it can be assumed that the generated velocity profiles do not represent the different flow states on a train roof
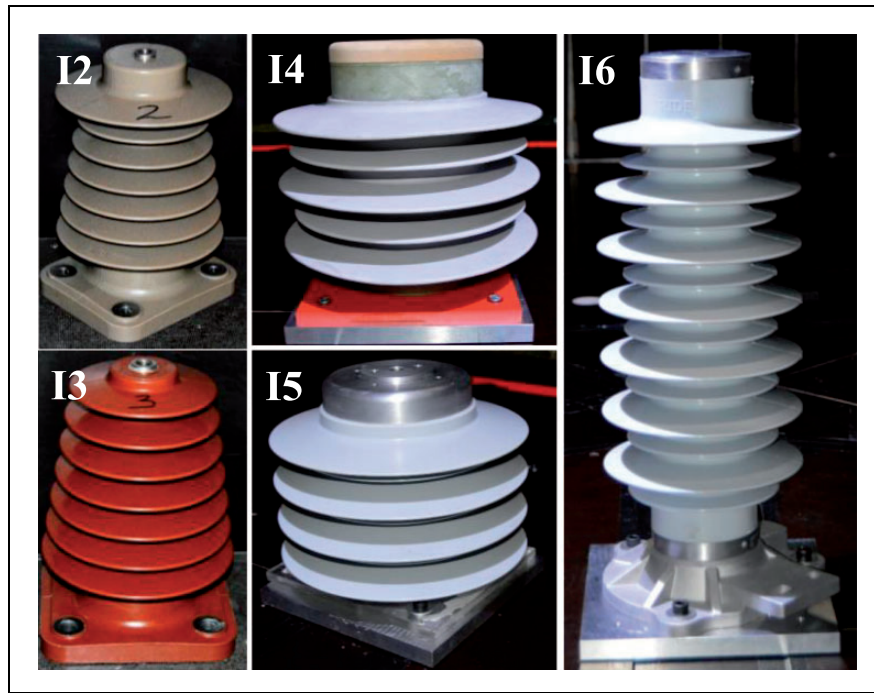
Figure 5. Investigated insulators: Insulator 2 (rigid resin); Insulator 3 (rigid resin); Insulator 4 (semi-rigid silicone); Insulator 5 (soft silicone); Insulator 6 (soft silicone). Insulator 1 is shown in Figure 4.

Table 1. Dimensions and properties of the different insulators and cylinders studied (overline indicates averaged values).

Object	$\overline{D_1}$ (m)	$\overline{D_2}$ (m)	H (m)	A_{proj} (m²)	D_{eff} (m) ($D_{eff}=A_{proj}/H$)	H/D_{eff}	Material
Cylinder	0.09	–	0.32	0.030	0.09	3.5	PVC
Cylinder	0.22	–	0.32	0.070	0.22	1.4	PVC
Insulator 1	0.09	0.21	0.32	0.035	0.11	2.9	CER
Insulator 2	0.11	0.19	0.32	0.040	0.13	2.5	CER
Insulator 3	0.11	0.18	0.30	0.037	0.12	2.5	CER
Insulator 4	0.17	0.28	0.25	0.051	0.20	1.3	HTV
Insulator 5	0.15	0.27	0.23	0.047	0.20	1.2	RTV
Insulator 6	0.10	0.18	0.55	0.067	0.12	4.6	LSR

CER: cycloaliphatic epoxy resin; PVC: polyvinyl chloride; HTV: High-Temperature-Vulcanizing silicone; RTV: Room-Temperature-Vulcanizing silicone; LSR: Liquid Silicone Rubber.

exactly, but to a good approximation. All velocity profiles were measured at 30 m/s and 60 m/s wind tunnel speed in order to evaluate the Reynolds number dependency of the respective flow pattern. Except for smaller variations in the velocity profiles measured close to the roofbox (i.e. x2, x3), no dependency on the Reynolds number, i.e. the flow velocity could be observed. Therefore, the flow conditions within the different boundary conditions investigated were supposed to be comparable at all Reynolds numbers investigated.

Drag coefficients

The drag coefficient C_D of the cylinders and the rigid insulators plotted against the Reynolds number is shown in Figure 9. The drag coefficient is given by

$$C_D = \frac{F_x}{p_{dyn}A_{proj}} \qquad (4)$$

with F_x being the force in the flow direction, p_{dyn} the dynamic pressure as detected by the Prandtl-tube, and A_{proj} the projected cross-sectional area of the respective object. The Reynolds number is defined using the effective diameter D_{eff} (Table 1)

$$Re_{D,eff} = \frac{uD_{eff}}{v} \qquad (5)$$

with u being the flow velocity measured by the Prandtl tube. Figure 7 shows the drag coefficient measured for
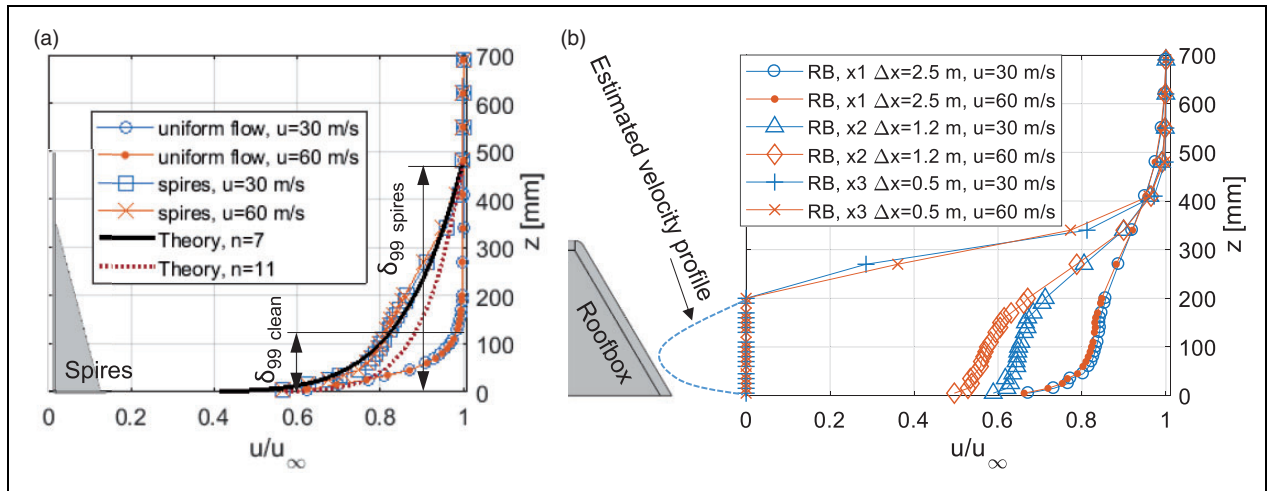
Figure 6. Measured and calculated boundary layer profiles: (a) for "undisturbed flow" and "spires" configuration and (b) "roofbox" configurations.
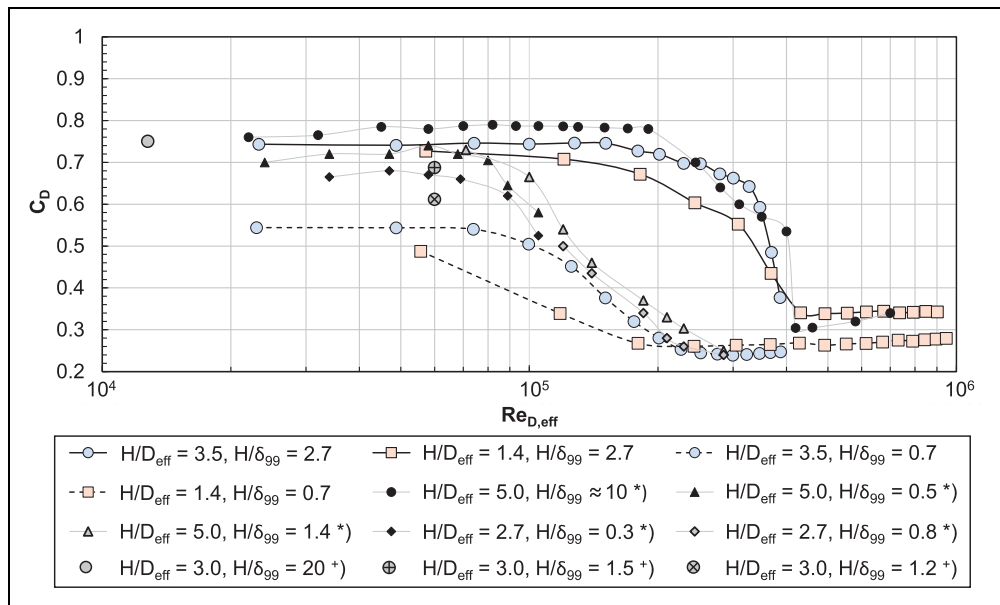

Figure 7. Drag coefficient of cylinders with different H/D ratios and boundary layer thicknesses plotted over the Reynolds number, compared to the results by Wang et al.[11]* and Sumner et al.[10+].

the cylinder with different H/D ratios and boundary layer thicknesses, compared to the results presented by Wang et al.[11] and Sumner et al.[10] The results correspond well with respect to the H/D ratio and boundary layer thickness. As expected, the drag coefficient experiences a drastic change when exceeding a critical Reynolds number of $Re_{D,eff} > 1$–2×10^5 and drops from $C_{D, subcritical} \approx 0.74$ (0.72 for the thicker cylinder) to $C_{D, supercritical} = 0.34$ (with thin boundary layer thickness applied). With increased boundary layer thickness (and probably turbulence in the near-wall flow), the laminar-turbulent transition shifts towards lower Reynolds numbers in the same way as observed by Wang et al.[11] As found by other studies,[10] an increase in the H/D ratio also increases the drag coefficient because a larger part of the object is exposed to the undisturbed flow. The strong impact of the aspect ratio becomes apparent when comparing the results for $H < \delta_{99}$ to the ones obtained by Wang et al.[11] The drag coefficient in the subcritical regime in the current study is significantly lower, even though the boundary layer profiles at the measurement position appear to be quite similar (cf. Figure 8). To a certain amount, the deviations at very low Reynolds numbers might as well be a result of measurement uncertainties for the very low forces in both studies.

Figure 9(a) shows the drag coefficient of the rigid insulators compared to the cylinder. Similar to the cylinder, the drag coefficient appears to be affected by the transition of laminar to turbulent flow. However, the change appears to be less sudden and the supercritical state probably could not be achieved

with the velocities applied. In general, the application of the sheds increases the drag coefficient slightly.

Figure 9(b) shows the drag coefficient for the insulators with flexible sheds. It can be seen that the drag coefficient again behaves qualitatively similar to the one of the cylinder. The drag coefficient of Insulator 4 (HTV) behaves similar to the ones of the rigid
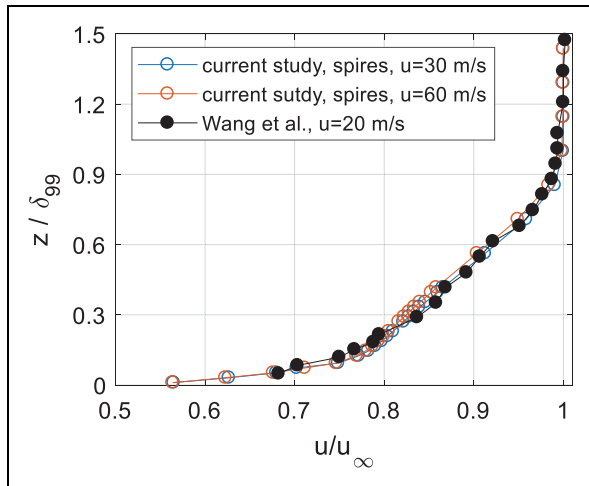

Figure 8. Boundary layer profiles as measured in the current study and that given by Wang et al.[11]

insulators and confirms that the supercritical drag with fins or sheds applied seems to be less decreased than for a bare cylinder. For the insulators with the very soft sheds (Insulators 5 and 6), the drag starts to increase strongly above a certain flow speed. This increase is due to the onset of fluttering of the sheds as can be observed in Figure 10. The displacement Δz of the sheds has been analyzed by video monitoring over a time span of 25 s using a *GoPro Hero4* at a framerate of 120 fps. The average maximum peak amplitude $\Delta z/2$ normalized by the projected shed radius r^* for different flow velocities is shown in Figure 11. It can be seen that the strongest displacement appears at maximum flow momentum conditions, i.e. the thin boundary layer case and the laterally displaced roofbox. For Insulator 4, no displacement could be observed (a slow onset might be indicated by the slight drag increase at highest flow speed), making it a rigid-body reference for Insulator 5. Unfortunately, for a more detailed analysis of the oscillation frequencies, both the camera and the balance appeared to have either too low resolution or stiffness. Therefore, only average quantities could be discussed.

Figure 12(a) to (c) shows the influence of the different upstream boundary conditions. For all insulators, a decrease of the critical Reynolds number, i.e.
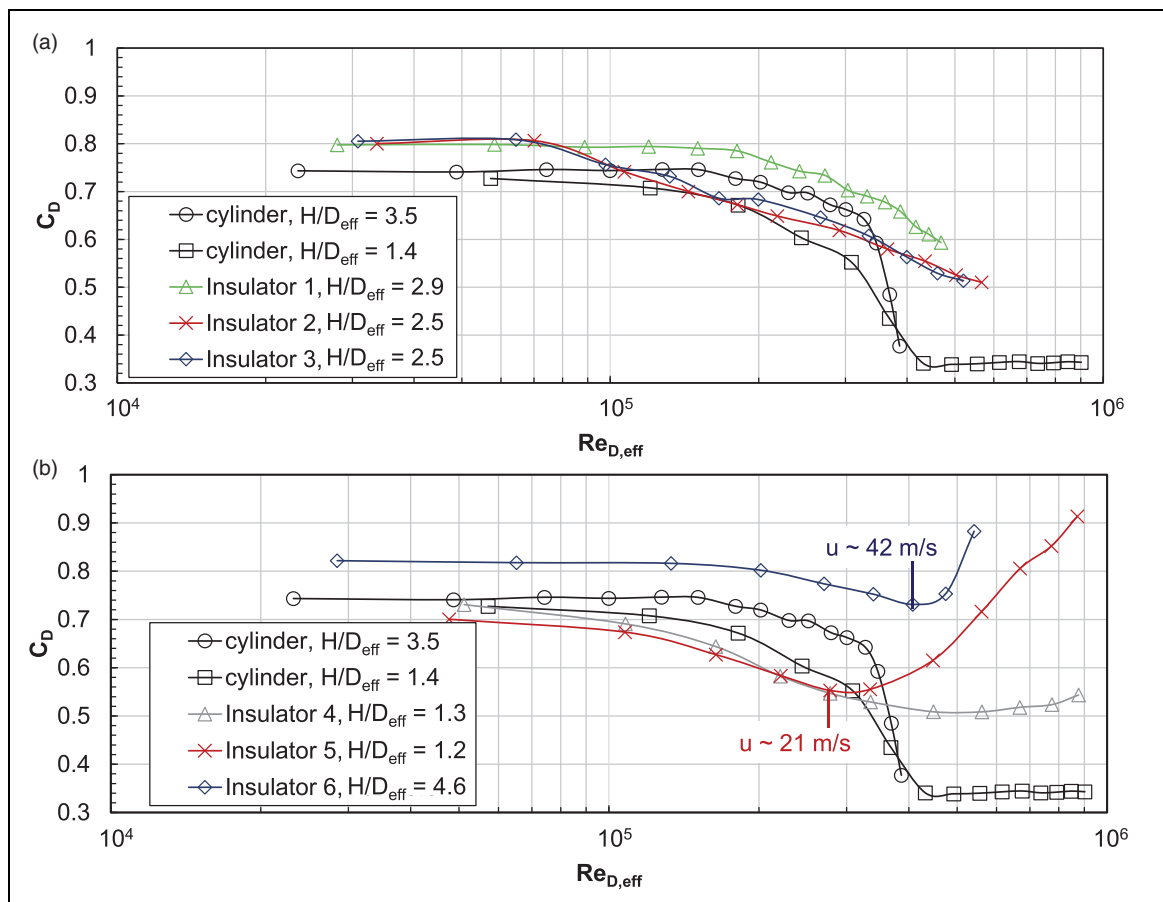

Figure 9. Drag coefficient of (a) cylinder and rigid insulators and (b) flexible insulators in "undisturbed flow" configuration.
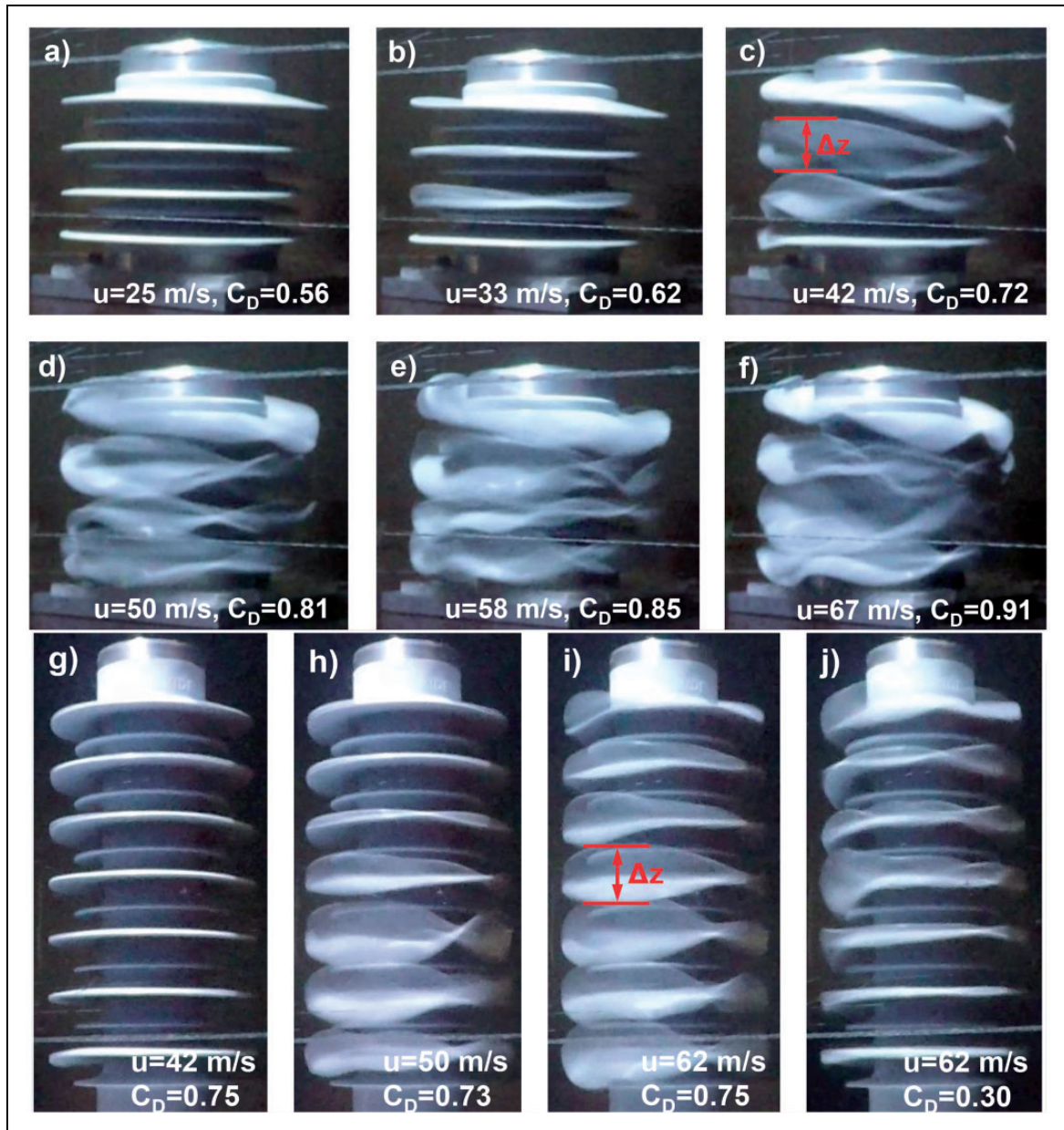
Figure 10. Snapshots of the shed displacement of Insulator 5 in undisturbed flow (a–f) and Insulator 6 in undisturbed flow (g–i) and behind roofbox x3 (j).
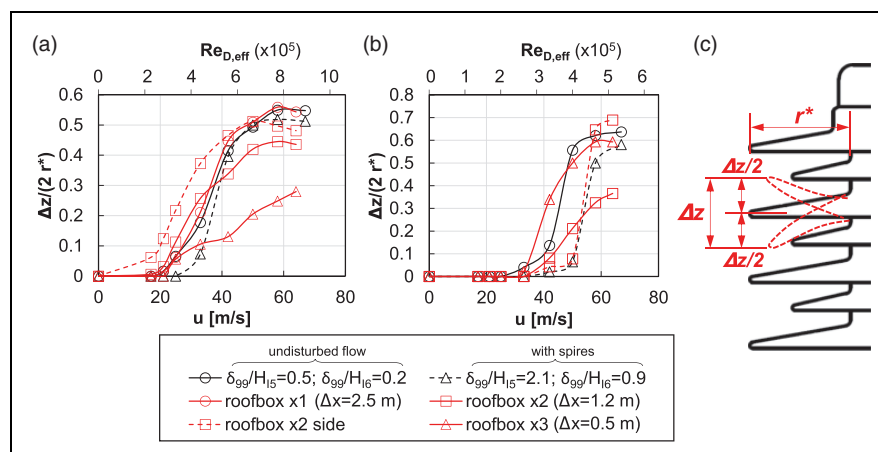

Figure 11. Shed displacement for (a) Insulator 5 ($r*/D_1 \approx 0.4$) and (b) Insulator 6 ($r*/D_1 \approx 0.5$); (c) sketch of insulator sheds.
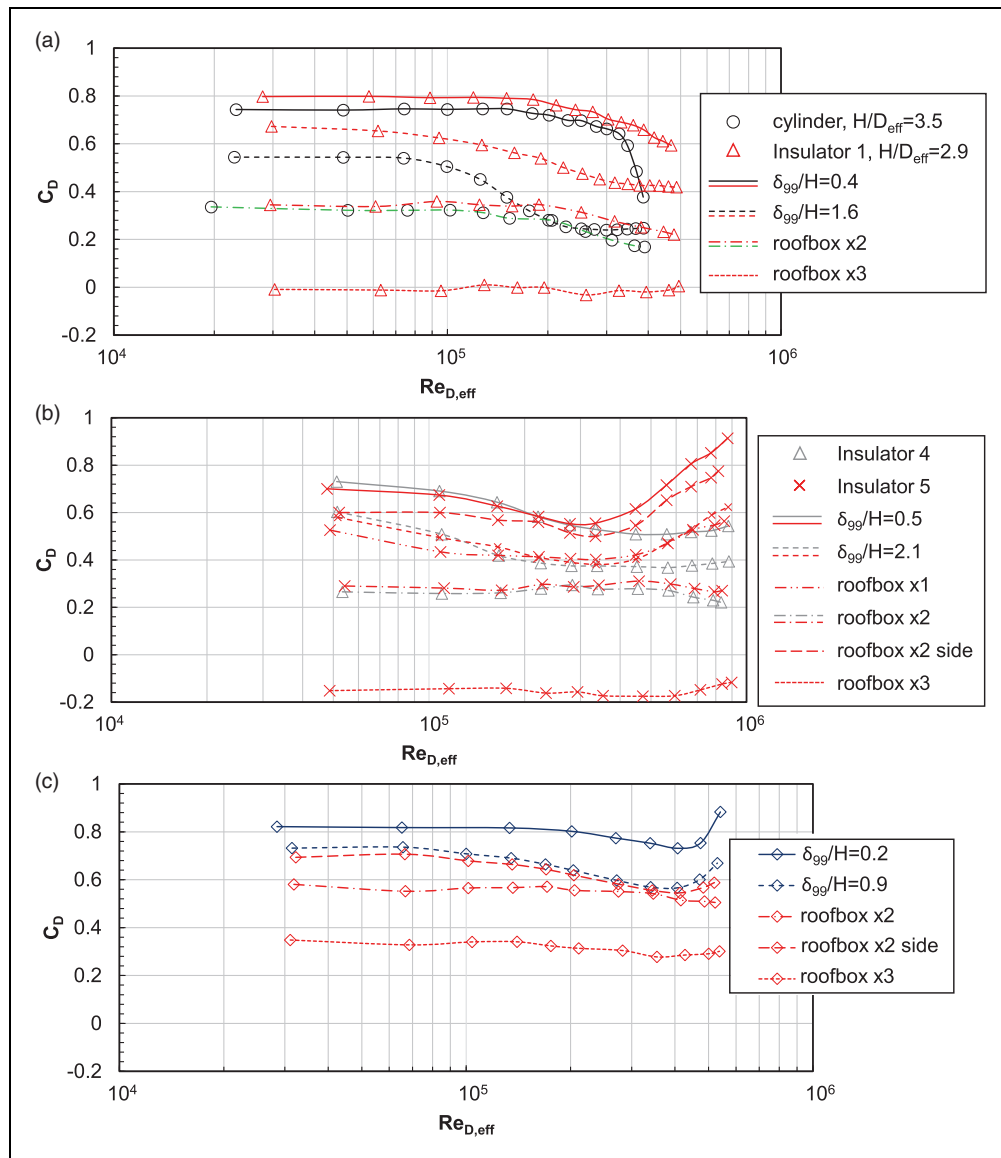
Figure 12. Drag coefficient at different boundary conditions of (a) cylinders and Insulator 1 (rigid), (b) Insulator 4 (semi-rigid) and Insulator 5 (flexible), and (c) Insulator 6 (flexible).

an earlier laminar-turbulent transition, can be observed with increasing boundary layer thickness (and probably near-wall turbulence). This observation agrees with the findings of Wang et al.[11] Generally, the drag coefficient decreases when the near-wall momentum flux is reduced, regardless of whether the spires or the roofbox are applied. In case of the smallest roofbox distance (x3), the backflow, as indicated in Figure 6, even causes a negative drag for the insulators with very low height (i.e. I5, cf. Figure 5). The drag increase due to oscillation of the sheds in all cases corresponds well with the amplitude observations presented in Figure 11. The lateral displaced roofbox (x2 side) seems to have nearly no shielding effect.

In case of insulators, which are partly covered by an upstream roofbox, only the sheltered sheds oscillate less than under free-stream conditions (Figure 10(j)). From the force and momentum

measurement of Insulator 6, the presence of the back-wash in case of the roofbox at position x3 (0.5 m upstream the insulator) could be confirmed, as the ratio of M_y/F_x increases by approximately 12% compared to the uniform flow conditions. The reversed flow direction in the lower part of the insulator increased the momentum around the y-axis.

Figure 13 also compares the lift coefficient (defined according to equation (4) using F_z instead of F_x) measured for Insulators 4 and 5. It can be seen, that the lift coefficient of the rigid and flexible variant behaves very similar to the drag coefficient. With the onset of shed oscillation, an increase of the lift can be observed as well. However, the lift coefficient appears to reach a maximum slightly below the maximum speed investigated and afterwards starts to decrease again, independent of the investigated boundary layer thickness. The absolute value of the lift coefficient might not be completely accurate due to influence of the connection
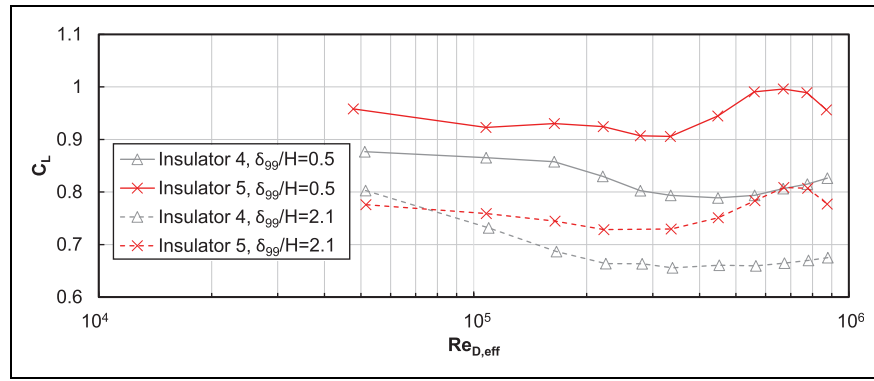
Figure 13. Lift coefficient of Insulator 4 (semi-rigid) and Insulator 5 (flexible) at different boundary conditions.
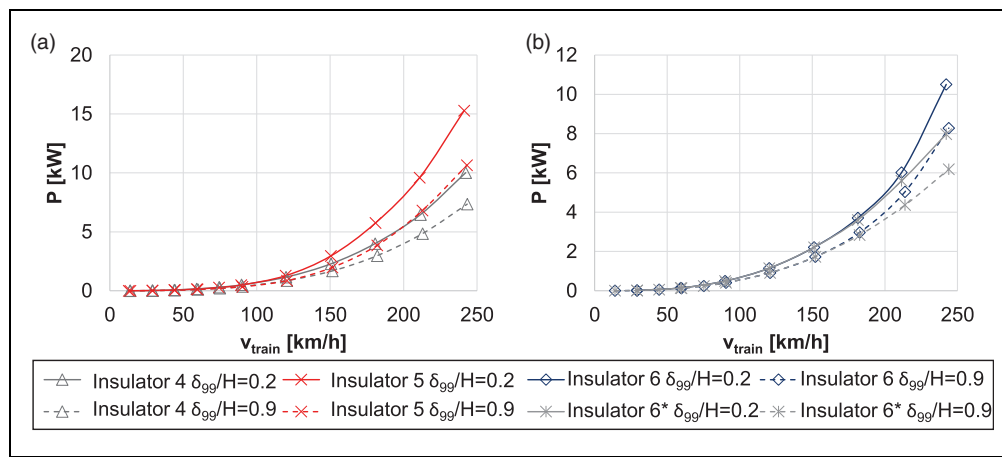

Figure 14. Required power at different train speeds for rigid-shed (Insulators 4 and 6*) and flexible-shed (Insulators 5 and 6) insulators (see note 'a') for different boundary layer thicknesses.

plate. Still, the impact of the shed material becomes clearly apparent.
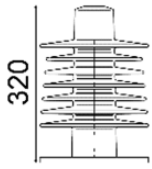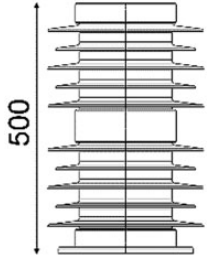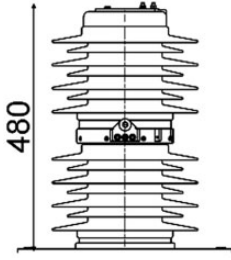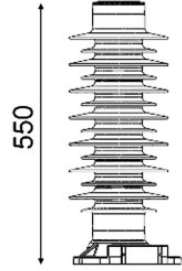
Impact on train energy demand

In the previous section, it was shown that the drag coefficient of an insulator strongly depends on boundary conditions such as upstream flow conditions and flow speed. Furthermore, it could be seen that the drag coefficient increases if the insulator exhibits flexible sheds, fluttering excited by the flow. Figure 14 shows the required power P to overcome the aerodynamic resistance of the insulators at the respective velocity v_{train}

$$P = F_D \cdot v_{train} = C_D \frac{\rho}{2} A v_{train}^3 \qquad (6)$$

It can be seen that the power demand of the flexible Insulator 5 for velocities above 130km/h is about 50% higher than for the nearly rigid Insulator 4, almost independent of the upstream boundary layer thickness and hence position on the train (as long as the insulator is not completely shielded by upstream roof

equipment), Figure 14(a). In Figure 14(b), the power demand for Insulator 6 compared to a fictive rigid variant 6* is shown. The additional power required due to the oscillating sheds can be assumed to be about 25% at highest velocity, while below 200 km/h no impact can be seen. Therefore, when directly exposed to the flow around a fast train, insulators with flexible sheds can significantly increase the required power to overcome the aerodynamic drag associated with the roof equipment. The proportion of the aerodynamic drag of a single insulator[a] in relation to the amount of the total train is given in Table 2, based on the drag coefficients measured for the respective velocity. Two types of trains are considered: one running at a top speed of 160 km/h (regional/commuter train) and one at 200 km/h (inter-city train). The average velocity of the trains is calculated using $v_{ave} = 0.5 \cdot v_{max}$ for the regional train (=80 km/h) and $v_{ave} = 0.65 \cdot v_{max}$ for the inter-city train (=130 km/h), based on the relations given by Ihme[29] and Garcia.[30] For both trains an aerodynamic drag coefficient of $C_{D,train} = 1$ is assumed, which approximately corresponds to the drag coefficient of a 200 m long inter-city or 120 m long regional

Table 2. Relation of aerodynamic drag of different insulators compared to the total train drag at different velocities.

	Insulator I	Insulator 4	Insulator 5	Insulator 6
	$C_{D,ins}/C_{D,train}$ at $v_{ave}=80$ km/h	$C_{D,ins}/C_{D,train}$ at $v_{ave}=80$ km/h	$C_{D,ins}/C_{D,train}$ at $v_{ave}=80$ km/h	$C_{D,ins}/C_{D,train}$ at $v_{ave}=80$ km/h
Undisturbed flow	0.28%	0.55%	0.52%	0.54%
Spires	0.20%	0.47%	0.45%	0.44%
Roofbox x2	0.12%	0.43%	0.40%	0.38%
	$C_{D,ins}/C_{D,train}$ at $v_{ave}=130$ km/h	$C_{D,ins}/C_{D,train}$ at $v_{ave}=130$ km/h	$C_{D,ins}/C_{D,train}$ at $v_{ave}=130$ km/h	$C_{D,ins}/C_{D,train}$ at $v_{ave}=130$ km/h
Undisturbed flow	0.26%	0.52%	0.61%	0.52%
Spires	0.16%	0.45%	0.51%	0.40%
Roofbox x2	0.11%	0.41%	0.45%	0.37%

train.[31] The reference area both for train and insulators was set to $A = 10\,\mathrm{m}^2$. It can be seen that a single insulator generates approximately 0.1–0.6% of the total train's aerodynamic resistance (and thus aerodynamic energy consumption) at average speed, strongly depending on its size and position on the train. Since the boundary layer thickness at the end of a 200 m long train probably exceeds the one considered in the current investigations, the drag contribution of elements placed at rear cars is likely to be a little below the values given in Table 2. Still these data can be used to get an impression about the expected drag generated by roof insulators. Exemplary two trains will be considered based on the data given in Table 2. The regional train BR425 (average speed 80 km/h) in double-traction is about 120 m long and in this configuration exhibits approximately 36 insulators of types 1 and four of type 4. For simplification, all of them are considered to be in the "roofbox x2" position. The aerodynamic resistance of the insulators then is approximately 6% of the total train's aerodynamic drag. At the average speed of 80 km/h, flexible insulator sheds would probably not cause any difference (compare Insulators 4 and 5, Table 2). The inter-city train BR411 (average speed 130 km/h) also has a length of about 200 m. Fourteen insulators of type 1 are placed around the pantographs as well as four insulators of type 4, which are considered as "roofbox x2" position. Additionally, 10 insulators of type 1 are placed along the train at both sides of the inter-car gaps, considered as "spires" position.

Using the values given in Table 2, the insulators contribute nearly 5% to the entire train's aerodynamic drag. In case of fluttering insulator sheds, this amount would further increase (Insulator 4 vs. Insulator 5, Table 2). These results agree well with the observations and estimations from other studies regarding the aerodynamic drag of roof components.[4–7] It confirms that the roof equipment, i.e. insulators, has a significant impact on a train's aerodynamic resistance, and design, material, as well as arrangement of the insulators, even at lower speeds, should be chosen advisedly.

Conclusion

In the present study, the aerodynamic drag of roof-mounted insulators was investigated. Different boundary conditions as found on the roof of trains were simulated. It could be shown that the drag coefficient behaves similar to that of a simple cylinder. A subcritical, critical, and supercritical Reynolds number regime could be observed for both cylinders and insulators, with a slightly lower difference in the drag coefficient between subcritical and supercritical drag and an extended critical regime for the insulators. Both the cylinder's and insulator's drag coefficient depend strongly on the upstream flow conditions. Furthermore, the impact of flexible insulator sheds was investigated. It could be observed that the insulators made of soft silicon (RTV, LSR) start to flutter above a certain inflow velocity, causing a strong

increase in the drag coefficient for higher flow/train speeds.

From the results of the investigation, the following can be concluded:

- roof elements such as insulators and surge arresters can be responsible for a considerable amount of a train's aerodynamic drag (about 5%),
- the drag contribution of each insulator strongly depends on its shape, material, and position on the train,
- in case of fluttering sheds, the drag of insulators increases strong enough to affect the entire train's aerodynamic drag.

Furthermore, the simulation of roof elements in studies regarding aerodynamic drag measurement should be considered carefully. Ignoring the influence of roof elements might result in a significantly underestimated drag coefficient. However, the strong impact of the Reynolds number requires a detailed analysis of scaling parameters, as in scaled experiments it is very likely only the subcritical regime can be investigated.

Regarding an analysis of the durability of the insulators with flexible sheds, it can be assumed that the increased converted energy in case of fluttering causes an accelerated aging of the insulators. The comparison of Insulators 4 to 6 shows that the onset of fluttering depends on material and geometry of the sheds (thickness of the sheds, diameter ratios). All of the three insulators are equipped with unsymmetrical and rather slim sheds, i.e. different curvatures on bottom and top side, which creates a lift force acting on the sheds. This lift is supposed to strongly support the onset of fluttering, especially on thin material. Therefore, besides using less flexible material, symmetrical-shaped sheds and a thicker design should be opted for an improved fluttering behavior.

ORCID iD

Jonathan Tschepe https://orcid.org/0000-0002-8674-9332

Note

a. For Insulators 4 and 5, the drag force has been calculated using $A = 2\,A_{proj}$ because the insulators in reality are twice as high as investigated in the wind tunnel (cf. Table 2). This implies a light underestimation of the drag coefficient compared to Insulator 6, as the boundary layer impact is doubled as well. Therefore, the upper part coefficient is considered as "undistorted flow" condition in all cases.

References

1. Peters J-L. Bestimmung des aerodynamischen Widerstandes des ICE/V im Tunnel und auf offener Strecke durch Auslaufversuche. *ETR* 1990; 39: 559–564.
2. Nolte R and Würtenberger F. *Evaluation of energy efficiency technologies for rolling stock and train operation of railways*. Berlin: UIC, 2003.
3. Lukaszewicz P. Running resistance - results and analysis of full-scale tests with passenger and freight trains in Sweden. *Proc IMechE, Part F: J Rail and Rapid Transit* 2007; 221: 183–193.
4. Gawthorpe RG. Train drag reduction from simple design changes. *Int J Veh Des* 1982; 3: 263–274.
5. Peters J-L. Aerodynamics of very high speed trains and maglev vehicles: state of the art and future potential. *Int J Veh Des* 1983; SP3: 308–341.
6. Peters J-L. Aerodynamische Gestaltung von Schienenfahrzeugen für den Schnellverkehr. *Archiv für Eisenbahntechnik*, 1985, pp.28–35.
7. Orellano A and Kirchhof R. Optimising the aerodynamics of high speed trains. *Railway Gazette Int* 2011; 41–45.
8. Rosemeier G. *Winddruckprobleme bei Bauwerken*. Berlin: Springer, 1976.
9. Farivar D. Turbulent uniform flow around cylinders of finite length. *AIAA J* 1981; 19: 275–281.
10. Sumner D, Heseltine JK and Dansereau OJP. Wake structure of a finite circular cylinder of small aspect ratio. *Exp Fluids* 2004; 37: 720–730.
11. Wang HF, Zhou Y and Mi J. Effects of aspect ratio on the drag of a wall-mounted finite-length cylinder in subcritical and critical regimes. *Exp Fluids* 2012; 53: 423–436.
12. Pattenden RJ, Turnock SR and Zhang X. Measurements of the flow over a low-aspect-ratio cylinder mounted on a ground plane. *Exp Fluids* 2005; 39: 10–21.
13. Roshko A. Experiments on the flow past a circular cylinder at very high Reynolds numbers. *J Fluid Mech* 1961; 10: 345–356.
14. Bearman PW. On vortex shedding from a circular cylinder in the critical Reynolds number regime. *J Fluid Mech* 1969; 37: 577–585.
15. Güven O, Farell C and Patel V. Surface-roughness effects on the mean flow past circular cylinders. *J Fluid Mech* 1980; 98: 673–701.
16. Hoerner SF. *Fluid-dynamic drag*. Bakersfiled, CA: Hoerner Fluid Dynamics, 1965.
17. Mair WA, Jones PDF and Palmer RKW. Vortex shedding from finned tubes. *J Sound Vib* 1975; 39: 293–296.

18. Ziada S, et al. The effect of fins on vortex shedding from a cylinder in cross-flow. *J Fluids Struct* 2005; 21: 689–705.

19. Khashehchi M, et al. A comparison between the wake behind finned and foamed circular cylinders in cross-flow. *Exp Therm Fluid Sci* 2014; 52: 328–338.

20. McClure J and Yarusevych S. Vortex shedding and structural loading characteristics of finned cylinders. *J Fluids Struct* 2016; 65: 138–154.

21. Takaishi T and Ikeda M. Experimental method for wind tunnel tests to simulate turbulent flow on the roof of high-speed trains. *QR RTRI* 2012; 53: 167–172.

22. Firchau W, Kiekebusch B and Neppert H. *Grenzschichtdaten für moderne Züge*. Ottobrunn: MBB, 1980. MBB TN HE 211 212 22 80.

23. Carnevale M, Facchinetti A and Rocchi D. Assessing aerodynamic effects on a railway pantograph by means of computational fluid dynamics. In: *Proceedings of the third international conference on railway technology*, Cagliari, Sardinia, Italy, 5-8 April 2016.

24. Irwin HPAH. The design of spires for wind simulation. *J Wind Eng Ind Aerodyn* 1981; 7: 361–366.

25. Schlichting H and Gersten K. *Boundary-layer theory*. Berlin: Springer-Verlag Berlin Heidelberg, 2000.

26. Neppert H. Komponenten-Widerstände im Einfluß der Grenzschicht an Zügen variabler Länge. *ZEV-Glasers Annalen* 1984; 9: 239–247.

27. Crespi P, Grégoire R and Vinson P. Laser Doppler velocimetry measurements and boundary layer survey on-board the TGV high-speed train. In: *Proceedings of the world congress on railway research*, 1994, Vol. 2, pp.767–773.

28. Carnevale M, et al. Computational fluid dynamics as a means of assessing the influence of aerodynamic forces on the mean contact force acting on a pantograph. *Proc IMechE, Part F: J Rail and Rapid Transit* 2016; 230: 1698–1713.

29. Ihme J. *Schienenfahrzeugtechnik*. Wiesbaden: Springer, 2016.

30. Garcia A. *High speed, energy consumption and emissions*. Paris: UIC Report, 2010.

31. Hucho WH. *Aerodynamik der stumpfen Körper*. Wiesbaden: Vieweg+Teubner, 2011.